THE JOURNAL OF PHYSICAL CHEMISTRY C

Article

Cite This: J. Phys. Chem. C 2019, 123, 11628−11638

pubs.acs.org/JPCC

Structure of Hydrated Kaolinite Edge Surfaces: DFT Results and Further Development of the ClayFF Classical Force Field with Metal−O−H Angle Bending Terms

Maxime Pouvreau,[†,‡] Jeffery A. Greathouse,*[,§] Randall T. Cygan,[§] and Andrey G. Kalinichev*[,†]

[†]Laboratoire SUBATECH, UMR 6457—Institut Mines-Télécom Atlantique, Université de Nantes, CNRS/IN2P3, 44307 Nantes, France

[‡]Department of Chemistry, Washington State University, Pullman, Washington 99164, United States

[§]Geochemistry Department, Sandia National Laboratories, P.O. Box 5800, MS 0754, Albuquerque, New Mexico 87185-0754, United States

Supporting Information

ABSTRACT: Toward the development of classical force fields for the accurate modeling of clay mineral-water systems, we have extended the use of metal−O−H (M−O−H) angle bending terms to describe surface Si−O−H bending for hydrated kaolinite edge structures. Kaolinite, comprising linked octahedral Al and tetrahedral Si sheets, provides a rigorous test by combining aluminol and silanol groups with water molecules in hydrated edge structures. Periodic density functional theory and classical force fields were used with molecular dynamics to evaluate the structure, dynamics, hydrogen bonding, and power spectra for deriving optimum bending force constants and optimal equilibrium angles. Cleavage energies derived from density functional theory molecular dynamics calculations indicate the relative stabilities of both AC_1 and AC_2 edge terminations of kaolinite where Si−OH and Al−(OH_2) or Si−OH, Al−OH, and Al−(OH_2) groups exist, respectively. Although not examined in this study, the new Si−O−H angle bending parameter should allow for improved modeling of hydroxylated surfaces of silica minerals such as quartz and cristobalite, as well as amorphous silica-based surfaces and potentially those of other silicate and aluminosilicate phases.

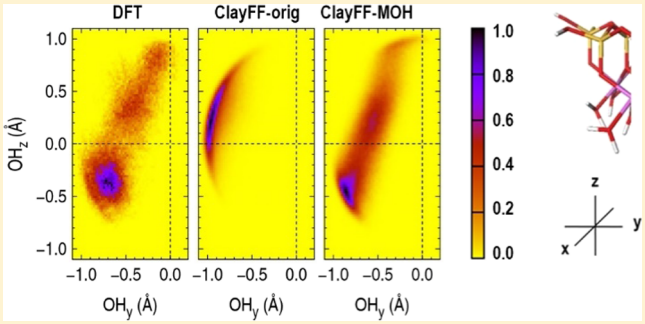

INTRODUCTION

Atomistic simulations of aluminosilicate clay minerals and related layered phases have seen widespread use over the past 20 years, providing molecular-level insight into structural and dynamic properties of their hydrated interlayers and interfaces for a wide variety of applications in fundamental science and engineering, including spectroscopic and structural characterization of clay interlayers and aqueous interfaces,[1−7] clay swelling phenomena and fossil energy extraction,[8−10] clay−polymer nanocomposites,[11−16] fate and transport of contaminants in the subsurface,[17−20] and underground disposal of waste products from energy production.[21−25] Many of the aforementioned simulation studies were performed at the classical level of theory using approximate energy expressions in the form of force fields (FFs). Large compositional and structural diversity of clays requires large system sizes and long time scales accessible with FF-based classical molecular dynamics (CMD) simulations to allow for the realistic computation of macroscopic observables such as structural parameters, transport properties, and adsorption properties. The continued use and success of clay-based FFs to predict experimentally accessible properties are due in large part to the development of robust, transferrable FFs specifically for layered minerals and their fluid interfaces.[26−31]

In the present study, we focus on ClayFF,[29] which consists primarily of nonbonded electrostatic and van der Waals interactions, allowing for efficient simulation while still maintaining natural flexibility within the clay layers. Framework flexibility is particularly important for accurately simulating molecular momentum transfer at the mineral−fluid interface. ClayFF has been used extensively to simulate bulk properties of clays and the interaction of fluids at their basal surfaces and interlayers. However, the extension of ClayFF to accurately model crystal edge surfaces requires a new parameterization of surface hydroxyl groups either already present in the crystal or satisfying dangling bonds as a result of mineral cleavage or growth/dissolution processes. In particular, M−O−H angle bending parameters (where M is a layer metal atom or cation such as Si, Al, or Mg) were not fully developed in the original parameter set.[29] At a minimum, an M−O−H

Received: January 17, 2019
Revised: February 27, 2019
Published: March 18, 2019

DOI: 10.1021/acs.jpcc.9b00514
J. Phys. Chem. C 2019, 123, 11628−11638

angle term prevents instabilities resulting from local structural disorder.[32−35] The strong hydrogen bonds (HBs) observed between hydroxyl groups at the edge surface by ab initio simulations in clay minerals[36] likely contribute to the overall cohesion of these surfaces. Similar to force field improvements that result in stronger M−O interactions,[37] the parameters that restrain the orientation of the edge hydroxyl groups act to mechanically stabilize the interfacial hydrogen bonds, thus preventing unphysical dissociation of surface hydroxyl groups into the fluid phase and allowing one to realistically model finite-size clay nanoparticles in classical atomistic simulations.

We have previously developed ClayFF-compatible M−O−H angle bending terms for Mg and Al atoms in octahedral coordination, guided by periodic quantum calculations using the density functional theory (DFT) on end-member layered phases brucite, $Mg(OH)_2$, and gibbsite, $Al(OH)_3$.[38,39] In this work, we continue the development of M−O−H angle bending terms for ClayFF—hereafter referred to as ClayFF-MOH—specifically for silanol (Si−O−H) groups that exist at cleaved surfaces of clay minerals containing siloxane sheets. In the evolution of our previous work, the structural models used for Si−O−H parametrization were based on the neutral end-member clay mineral kaolinite.

Kaolinite, $Al_2Si_2O_5(OH)_4$, occurs extensively in numerous soil and sedimentary environments and has a significant impact on many geochemical, environmental, and technological applications primarily due to its occurrence and stability under a broad range of temperature, pressure, and chemical conditions.[40] Like all phyllosilicate clay minerals, kaolinite is characterized by a polymerized structure of SiO_4 tetrahedra (T) occurring as a siloxane sheet, which, in the case of kaolinite, is linked to a single sheet of $AlO_4(OH)_2$ octahedra (O) to form a repetitive TO layered structure. Only two of the three available octahedral sites in the Al sheet are occupied, thereby leading to the dioctahedral designation.[41] The coordination environment of each Al includes one inner hydroxyl group and three hydroxyl groups on the basal surface. Typically exhibiting ideal stoichiometry and with limited impurities, kaolinite has no net layer charge. Hydrogen bonds between basal hydroxyl groups of the O sheet and the basal siloxane oxygens of the T sheet result in stable TO−TO interactions that ultimately create the booklike crystal habit extending along the *c*-axis.[41] The hexagonal-based atomic ring structures of the Si(T) and Al(O) sheets result in hexagonally shaped macroscopic crystals with terminating edge structures that are the main focus of this computational study.

It has been understood for quite some time that edge sites contribute strongly to kaolinite surface area and charge development.[42] Several periodic DFT studies have examined adsorption and chemical properties of cleaved edge surfaces of kaolinite. Kremleva et al.[43] modeled the adsorption of UO_2^{2+} ions on the (010) edge surface in the presence of a monolayer of water. Their preliminary calculations determined that the most stable protonation state at the edge consists of one Al atom per unit cell coordinated by one OH group and one OH_2 group,[43] which is consistent with the model edge surface used in the present study. The relative stabilities of various terminations of edge surfaces exposed to water have been studied by Liu and co-workers using DFT-MD simulations initially to determine stable coordination environments for edge Al and Si atoms[44] as well as surface pK_a values.[45] These studies provide insights into the local coordination environment at hydrated kaolinite edges under different pH conditions, which will aid in the construction of model surfaces for FF simulations of kaolinite−water interfaces. Although the surface chemistry must remain fixed during FF simulations, interfacial properties at larger scales can be modeled at different solution or pH conditions based on the DFT-predicted protonation states.

Our methodology in developing and testing Si−O−H angle bending parameters is similar to that in our previous works on octahedrally coordinated metal atoms (Al−O−H and Mg−O−H).[38,39] The new Si−O−H angle bending parameters are derived for kaolinite edges based on comparisons of structural and vibrational properties of edge silanol groups with the results of DFT-MD simulations. Additional validation is provided through detailed comparisons of hydrogen bonding properties at hydrated kaolinite edges, demonstrating the compatibility of multiple M−O−H angle terms in the same energy expression.

STRUCTURAL MODELS AND EDGE TERMINATIONS

The unit cell of the kaolinite $Al_2Si_2O_5(OH)_4$ crystal was constructed based on the X-ray diffraction data of Neder et al., which provides cell parameters of 5.15 × 8.94 × 7.40 Å^3, α = 91.69°, γ = 104.61°, and β = 89.82°.[46] The positions of hydrogen atoms and the orientations of the structural OH groups were further verified using neutron powder diffraction data.[47] The edge models of kaolinite were built from this unit cell by cleaving the bulk crystal along the corresponding crystallographic plane.

The most commonly observed kaolinite edge surfaces are (010), (110), and $(1\bar{1}0)$.[48] The (010) edge model was built from a 2 × 1 × 2 supercell cleaved along the corresponding planes. To build the (110) and $(1\bar{1}0)$ edge models, the unit cell was doubled along the [001] direction and multiplied along the direction orthogonal to the cleavage plane by a factor to obtain the same bulk formula as the (010) edge model (i.e., $Al_8Si_8O_{20}(OH)_{16}$). The cleavage planes were slightly translated with respect to the crystal structure to minimize the number of dangling bonds, which revealed the (010) and (110) edge models as structurally equivalent and correspond to the AC chain type, whereas the $(1\bar{1}0)$ surface corresponds to the B chain type.[49] Both edge types have been featured in the published DFT studies of kaolinite edge structures.[43−45] The AC- and B-edge models and the bulk supercell were equilibrated using DFT-MD *NVT*-ensemble simulations (number of particles *N*, volume *V*, temperature *T* = 300 K), and average energies were obtained from subsequent constant potential energy (*E*) *NVE*-ensemble simulations (Table 1). Reorientations of the hydroxyl groups were readily observed at this temperature, and sampling these various configurations

Table 1. Energies of Cleavage (ΔE_{cleav}) and Water Desorption ($\Delta E_{desorp}^{H_2O}$) for the Two Types of Kaolinite Edge Surfaces, Calculated as Averages of Total Energies at *T* = 300 K from *NVE*-Ensemble DFT-MD Simulations[a]

edge type	edge surface area (Å^2)	ΔE_{cleav} (kcal mol^{-1} Å^{-2})
AC[b]	295	0.032
B[c]	213	0.140

[a]Refer to Figure 1 for the corresponding snapshots. [b]Equivalent to (110). [c]A water molecule is spontaneously desorbed during equilibration.

DOI: 10.1021/acs.jpcc.9b00514
J. Phys. Chem. C 2019, 123, 11628−11638

leads to a more realistic estimation of the surface energy than the static approach.

DFT-MD snapshots of the AC- and B-edges are shown in Figure 1. During equilibration, a water molecule is

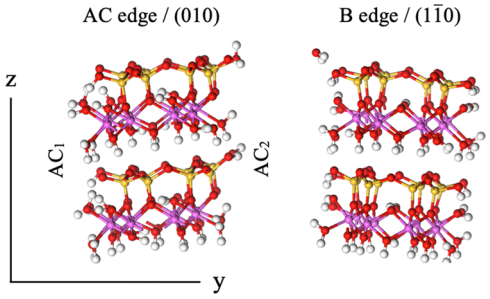

Figure 1. Kaolinite dry edge surfaces: snapshots from DFT-MD. Yellow, Si atoms; pink, Al atoms; red, O atoms; white, H atoms. The axes refer to the AC-edge model only.

spontaneously desorbed from a B-edge Al site while all the AC-edge Al sites remain 6-coordinated. The cleavage energies per surface area are defined as

$$\Delta E_{cleav} = \frac{E_{edge} - (E_{bulk} + nE_{H_2O,\,gas})}{A} \quad (1)$$

where E_{edge}, E_{bulk}, and $E_{H_2O,gas}$ are the DFT-MD average energies obtained, respectively, for the edge models, the bulk model, and an isolated water molecule in a 15 × 15 × 15 Å^3 box, and A is the total surface area of the respective edge model.

The dangling bonds were satisfied using chemi- or physisorption of H_2O molecules to obtain bulklike AlO_6 and SiO_4 coordinations, resulting in a zero net charge. In the periodic model, adjacent mineral slabs were separated by a 15 Å vacuum region. The resulting AC_1 surface was terminated by SiOH and Al(OH)(OH_2) groups, and the resulting AC_2 and B surfaces were terminated by SiOH and Al(OH_2) groups. The cleavage energies of the AC- and B-edge models are, respectively, 0.032 and 0.140 kcal mol^{-1} Å^{-2}. Therefore, we selected the kaolinite AC-edge as a representative structural model. According to the free energy calculations of Liu et al.,[44] for a neutral model, an AC_2 surface—"(110)-2" in their paper—will consist of both 5- and 6-coordinated Al sites, whereas an AC_1 surface—"(110)-1" in their paper—essentially consists of 6-coordinated Al sites. According to their pK_a calculations,[45] kaolinite edge surfaces consisting of SiOH and Al(OH)(OH_2) forms are likely to exist in neutral or moderately acidic conditions due to their respective pK_a values of 6.9 and 5.7.

Two model sizes were considered for subsequent calculations. The preliminary static calculations and the DFT-MD simulations were based on a 2 × 1 × 2 supercell, and the CMD simulations were based on a 4 × 2 × 4 supercell. To represent the complexity of a mineral surface consisting of 5- and 6-coordinated Al sites with a certain spatial distribution, the size of the model needs to be sufficiently large, which is not the case of the 2 × 1 × 2 supercell. Therefore, all Al atoms on the AC_1 edge surface were coordinated by one OH group and one OH_2 group.

METHODS

DFT. Periodic DFT calculations used the Perdew–Burke–Ernzerhof functional and the D3 dispersion corrections of Grimme et al.[50] The Gaussian and plane wave (GPW) scheme[51] was used with a split-valence double-zeta basis set using a single set of polarization functions,[52] Goedecker–Tetter–Hutter pseudopotentials,[53] and a plane wave cutoff of 350 Ry for the density grid. Together with the plane wave cutoff, additional GPW settings (relative cutoff, SCF convergence criterion, precision in the calculation of the Kohn–Sham matrix) enabled a small error in the calculated forces (<10^{-4}). The wave function was sampled at the Γ point. CP2K software[51] was used for all DFT calculations.

Force Field Parameters. For classical MD simulations, all FF parameters, except for the Si–O–H bending term, are presented in Table 2. The nonbonded parameters were taken

Table 2. Force Field Parameters

nonbonded[a]: $E_{nonbonded} = \frac{q_i q_j}{4\pi\epsilon_0 r} + 4\epsilon_{ij}\left[\left(\frac{\sigma_{ij}}{r}\right)^{12} - \left(\frac{\sigma_{ij}}{r}\right)^{6}\right]$				
species	atom type	q (e)	ε (kcal mol^{-1})	σ (Å)
tetrahedral Si	st	2.1000		
octahedral Al	ao	1.5750	1.3298 × 10^{-6}	4.2718
hydroxyl O	oh	−0.9500	0.1554	3.1655
hydroxyl H	ho	0.4250	0.000	0.0000
water O	o*	−0.8200	0.1554	3.1655
water H	h*	0.4100	0.0000	0.0000
$E^{bond}_{Morse} = D_0[1 - e^{-\alpha(r-r_0)}]^2$				
bond	D_0 (kcal mol^{-1})		α (Å^{-1})	r_0 (Å)
oh-ho[b]	132.2491		2.1350	0.9450
$E^{bond}_{harmonic} = k(r - r_0)^2$				
bond	k (kcal mol^{-1} Å^{-2})			r_0 (Å)
o*-h*[c]	554.13			1.0000
$E^{angle}_{harmonic} = k(\theta - \theta_0)^2$				
angle	k (kcal mol^{-1} rad^{-2})			θ_0 (deg)
h*-o*-h*[c]	45.770			109.47
ao-oh-ho[d]	15			110

[a]Original ClayFF parameters[29] with $\sigma_{\alpha\beta} = 1/2(\sigma_\alpha\sigma_\beta)$ and $\varepsilon_{\alpha\beta} = (\varepsilon_\alpha\varepsilon_\beta)^{1/2}$. [b]Set for dioctahedral clays.[54] [c]Ref 56. [d]Ref 39.

from the original ClayFF parameterization.[29] The original harmonic O–H-bond terms for the structural hydroxyl groups were replaced here with a more accurate Morse potential.[54] H_2O molecules—including the OH_2 groups attached to the Al atoms at the edges—are described by the SPC water model[55] with harmonic O–H bond stretching and H–O–H angle bending terms.[56] The already parameterized Al–O–H term was applied to kaolinite Al–OH groups and not to the Al–OH_2 groups because of the potential desorption of OH_2 groups, observed in our previous work for gibbsite edges.[39] Ewald summation was used with a cutoff distance of 10 Å, the same value being used for the Lennard-Jones terms.

Parametrization of the Si–O–H Bending Term. The Si–O–H bending term was parameterized in the functional form of

$$E_{bend} = k(\theta - \theta_0)^2 \quad (2)$$

where θ is the angle ∠Si–O–H and k is the bending force constant. The algorithm of parametrization was identical to the one used previously for the Al–O–H and Mg–O–H bending

DOI: 10.1021/acs.jpcc.9b00514
J. Phys. Chem. C 2019, 123, 11628–11638

terms[39] and consisted of finding the values of k and θ_0, which minimized the differences between the results of DFT and classical ClayFF-MOH calculations.

First, Γ-point vibrational modes were calculated using DFT for a given structure after a local geometry optimization. Then, using ClayFF-MOH and GULP software,[57] a local geometry optimization was performed starting from the DFT-optimized structure, followed by the calculation of Γ-point vibrational modes. These calculations were performed for every value of θ_0 within the 90−130° range ($\delta\theta$ = 1°) and for every value of k within the 0−40 kcal mol^{-1} rad^{-2} range (δk = 1 kcal mol^{-1} rad^{-2}), while all other ClayFF parameters were kept fixed. At the last stage, from the final structures and vibrational normal modes obtained for every pair of parameters (θ_0, k), absolute differences between DFT- and ClayFF-MOH-derived properties were calculated in terms of wavenumbers and in terms of O−H orientations. The optimization procedure is described in further detail in the Supporting Information of ref 39. The differences in terms of vibrational frequencies $\langle|\Delta\bar{\nu}|\rangle$ were also computed but were not found statistically meaningful due to a high standard error and thus not conclusive.[39]

It is important to keep in mind that the model edge surfaces used in the static calculations were hydrated by only one water layer. The surface relaxation of the edge O−H groups and their interaction with liquid water should create additional disorder, thus additional entropic effects. Therefore, the values of the parameters derived from the static energy minimizations are informative but may not necessarily be optimal when all thermodynamic effects are included. In the simulations, we have also tested a few other sets of (θ_0, k) values along with the optimized ones.

Molecular Dynamics. MD simulations were performed at T = 300 K using a time step of 0.5 fs. DFT Born−Oppenheimer molecular dynamics simulations (DFT-MDs) were used for the small structural models. LAMMPS software,[58] incorporating ClayFF with and without the Al−O−H and Si−O−H bending terms, was used in CMD modeling of larger simulations cells of kaolinite.

Lattice parameters of the large triclinic kaolinite bulk cells were relaxed during CMD simulations in the *NPT* ensemble at P = 1 bar using the Nosé−Hoover chain thermostat[59] and the Parrinello−Rahman barostat,[60] whereas the small bulk cells were relaxed using DFT cell optimizations. To obtain equilibrium water density in interfacial simulations, the pores of the small and large edge surface models were filled with 73 and 520 water molecules, respectively. Then, the dimension orthogonal to the surface (direction y according to the convention of Figure 1) was relaxed by performing *NPT*-ensemble CMD runs on both models for 1 ns, leading up to average equilibrium box lengths along y of 24.3 and 46.0 Å, respectively. The other two dimensions were derived from the simulations of the bulk crystal cells. After a final equilibration of atomic positions and velocities from *NVT* simulations for 2 ns (CMD) and 20 ps (DFT-MD), production runs were performed in the *NVE* ensemble for 100 ps (CMD) and 40 ps (DFT-MD), collecting atomic positions and velocities every 1 fs. Monitoring the radial distribution functions of the interface atoms over 10 separate windows of 100 ps at equilibrium CMD simulations, no difference was observed, confirming that equilibrium was attained and assuring the convergence of the ensemble averages. By dividing the DFT-MD trajectory into two windows of 20 ps and doing a similar comparison, no significant difference was observed within the statistical uncertainty. During the course of the *NVE*-ensemble simulations, the average temperature remained constant within 295−305 K.

RESULTS AND DISCUSSION

Static Calculations. To estimate the optimal values of the equilibrium angle θ_0 and the force constant k for the Si−O−H bending term, the average absolute difference between DFT and ClayFF-MOH OH orientations was compared. Absolute differences for each parameter are shown in Figure 2 for the kaolinite AC-edge model with one water layer on the AC_1 and AC_2 surfaces. The differences obtained from the AC_1 and AC_2 surfaces are averaged.

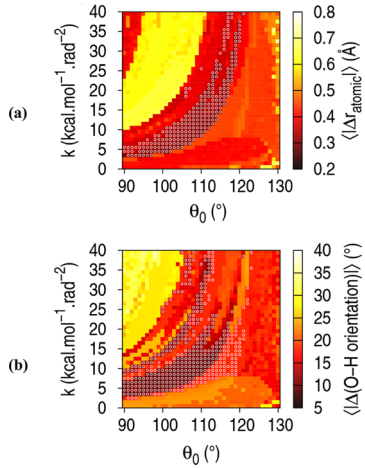

Figure 2. Optimization of the k and θ_0 values for the Si−O−H angle bending term from the maps of mean differences between DFT and ClayFF-MOH results in terms of (a) atomic positions and (b) O−H orientation on the kaolinite AC-edge surfaces. The outermost atoms of the two AC-edge surfaces are considered in the mean. The pixels with white circles represent the areas of minimal difference.[39]

For Si−O−H angle bending, (k, θ_0) areas leading to the minimal differences—represented by white dots—are quite large, leaving room for compromise with previously reported M−O−H parameters. The parametrized equilibrium angles for Mg−O−H and Al−O−H are $\theta_{0,MgOH}$ = $\theta_{0,AlOH}$ = 110°. Figure 2 shows that along the line θ_0 = 110°, the Si−O−H k range leading to the minimal $\langle|\Delta r_{atomic}|\rangle$ and $\langle|\Delta O{-}H_{orientation}|\rangle$ values are 8−18 and 7−18 kcal mol^{-1} rad^{-2}, respectively. Since the value k_{AlOH} = 15 kcal mol^{-1} rad^{-2} is within this range, it can a priori be used for the Si−O−H term. In the following, the values [$\theta_{0,SiOH}$ = 110°; k_{SiOH} = 15 kcal mol^{-1} rad^{-2}] will be used for ClayFF-MOH in the CMD simulations. Alternative parameters will be tested if the comparison between DFT-MD and CMD data reveals a possibility for improvement.

Proton Transfer. Snapshots from DFT-MD simulations of the hydrated AC surfaces are shown in Figure 3. While no proton exchange was observed between surface hydroxyl groups and interfacial water molecules, multiple proton transfer events occurred at the edge surfaces of kaolinite in DFT-MD simulations between silanol groups and neighboring aluminol groups: two Si−O−H groups out of four periodically deprotonated, exchanging the proton with the neighboring Al−O−H group. The proton residence times on either of the sites ranged from 5 to 10 fs. A snapshot from the DFT-MD simulation of the AC_2 surface is shown in Figure 3c, illustrating

DOI: 10.1021/acs.jpcc.9b00514
J. Phys. Chem. C 2019, 123, 11628−11638

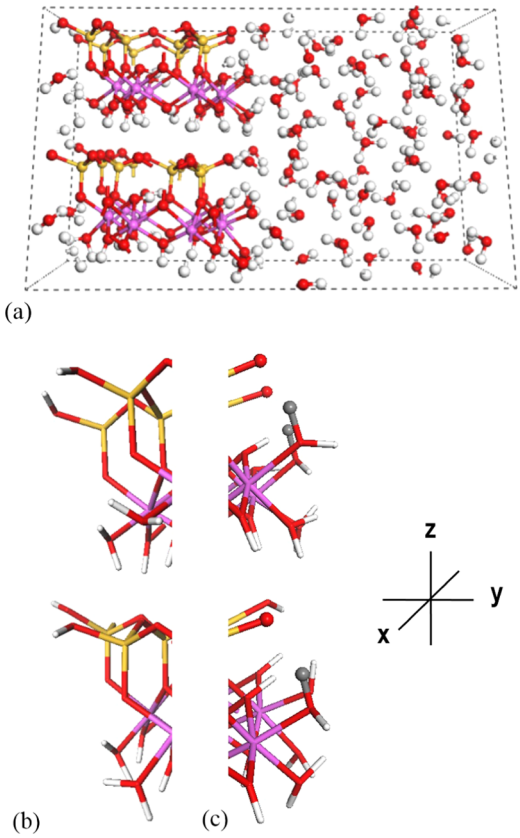

Figure 3. Snapshots from DFT-MD simulations of the (a) hydrated AC surface, (b) AC_1 surface, and (c) AC_2 surface. In the initial configuration (a) the surface consists of 4 SiOH sites and 4 $Al(OH)(OH_2)$ sites. In this snapshot, the surface is terminated by 1 SiOH, 1 $Al(OH)(OH_2)$, 3 SiO− and 3 $Al(OH_2)(OH_2)$ sites; the atoms represented by gray balls illustrate the proton transfers from the SiOH groups to the AlOH groups. Axes are shown for comparison with Figure 5.

the edge termination after a proton hopping event. To calculate MD-derived structural properties, for each configuration from the DFT-MD trajectory, OH and OH_2 groups were identified based on an O−H distance cutoff of 1.2 Å. Such proton transfer events are of course not possible in CMD simulations using ClayFF. The (static) distribution of protonated sites of a surface must be determined as an initial configuration for CMD simulations depending on factors such as fluid components and the desired pH.

Metal−O−H Angle and O−H Bond Orientation of Edge Hydroxyl Groups. The metal−O−H angle (∠MOH) distribution is a convenient first indicator of the bending term performance, in terms of both the angle of maximum probability and the amplitude of the metal−O−H bending (Figure 4). A more useful descriptor of surface hydroxyls is the absolute orientation of the O−H bond, shown as distributions of the OH vector in the *yz* plane in Figure 5. Here, *z* is the direction of the stacking of the tetrahedral and octahedral sheets and *x* is the direction orthogonal to the surface (Figure 3).

Silanol Groups. The Si−O−H angles corresponding to the maxima of the distributions of the AC_1 and AC_2 edge surfaces obtained by DFT-MD are $\angle SiOH^{max}$ = 119° and $\angle SiOH^{max}$ = 107°, respectively, with their full width at half-maximum (FWHM), respectively, at 18.1 and 13.5°. The distribution for

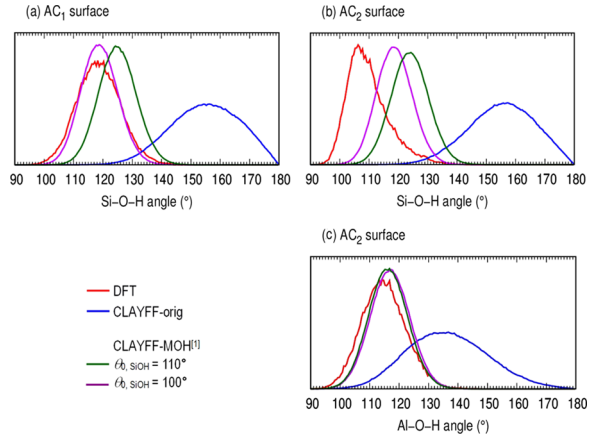

Figure 4. ∠Si−O−H and ∠Al−O−H angle distributions for the OH groups on the kaolinite AC_1 (a) and AC_2 (b), (c) edge surfaces. On the AC_1 surface, all Al atoms are coordinated to OH_2 groups only.[1] $\theta_{0,AlOH}$ = 110° and k_{SiOH} = k_{AlOH} = 15 kcal mol^{-1} rad^{-2}.

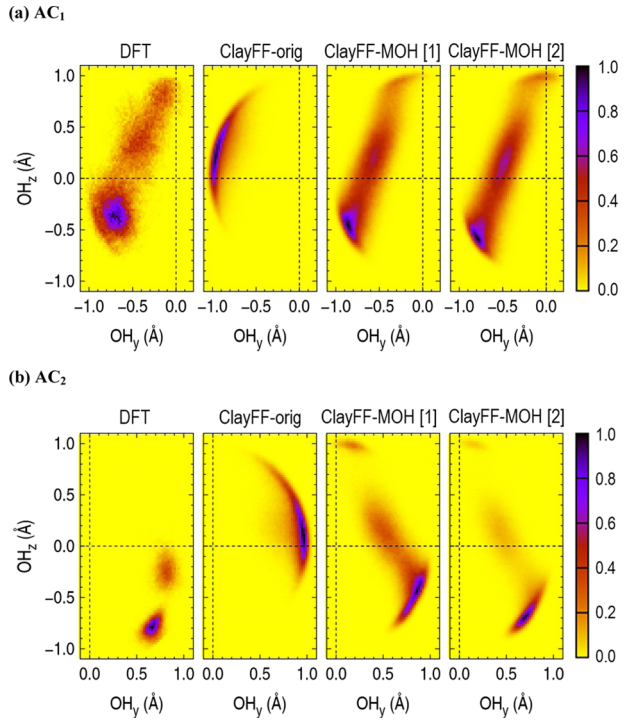

Figure 5. Orientation of the kaolinite Si−O−H belonging to the AC_1 and AC_2 edge surfaces. The distribution of the O−H bond vectors projected on the *yz* crystallographic plane from DFT, ClayFF-orig, and ClayFF-MOH MD simulations. The color range from the lowest to the highest intensity is yellow, red, and black.[1] $\theta_{0,SiOH}$ = 110° and k_{SiOH} = k_{AlOH} = 15 kcal mol^{-1} rad^{-2}.[2] $\theta_{0,SiOH}$ = 100° and k_{SiOH} = k_{AlOH} = 15 kcal mol^{-1} rad^{-2}.

the AC_2 surface is noticeably asymmetric, exhibiting a shoulder due to a secondary distribution centered approximately around 110°.

As seen in Figure 5a and illustrated in Figure 3b, the Si−O−H groups on the AC_1 surface are subject to reorientations during the simulation with a seemingly continuous orientation pattern in the *yz* plane, whereas the most probable orientation is at $y \sim -0.7$ Å, $z \sim -0.4$ Å. However, the Si−O−H groups on the AC_2 surface adopt two distinct and more restrained

DOI: 10.1021/acs.jpcc.9b00514
J. Phys. Chem. C 2019, 123, 11628−11638

orientations, the most probable of them being at y = +0.7 Å, z = −0.8 Å.

The distributions obtained with CMD without M−O−H terms (ClayFF-orig) have a very small overlap with the DFT-MD distribution due to the much more obtuse ∠SiOH^{max} angle at 156°. The distributions are also broader with their FWHM values almost doubled in extent. Using ClayFF-MOH with the angle bending parameters deduced from the static calculations ($\theta_{0,SiOH}$ = 110° and k_{SiOH} = 15 kcal mol^{-1} rad^{-2}) clearly narrows the distribution and brings it much closer to the DFT-MD results, with FWHM values of 16 and 15°, respectively, for the AC_1 and AC_2 surfaces. However, the distributions are centered around ∠SiOH^{max} = 125° for the two surfaces. While the ∠SiOH^{max} difference of the results for the AC_1 surface is around 6°, the difference of 18° for the AC_2 surface is less acceptable. Therefore, we performed CMD simulations with a lower value of the Si−O−H equilibrium angle θ_0 = 100° for ClayFF-MOH to evaluate its effect on the ∠SiOH distribution. As a result, the distributions are shifted to lower angles of 118 and 117°, that is, significantly closer to the DFT-MD values for both the AC_1 and AC_2 surfaces (Figure 4a,b).

These improvements in terms of angular distributions translate into more realistic O−H orientations as seen in Figure 5. On the AC_1 surface, the region of higher probability O−H orientation predicted by ClayFF-MOH agrees well with DFT-MD, with the most probable orientation being in the lower left quadrant in the yz plane ($y \sim -0.8$ to -0.9 Å, $z \sim -0.5$ to 0.6 Å) and extending along a segment until the $+z$ orientation ($y \sim 0$, $z \sim 1.0$ Å). On the AC_2 surface, while the agreement between ClayFF-MOH and DFT-MD results is less pronounced, the region of the most probable Si−O−H orientations in the $+y$, $-z$ quadrant is significantly improved compared to the performance of ClayFF-orig.

Aluminol Groups. Similar to the gibbsite (100) edge surface in our previous work,[39] Figure 4c shows that the Al−O−H term dramatically improves the corresponding angle distribution on the AC_2 surface. The agreement between DFT-MD and ClayFF-MOH is clear, with ∠AlOH^{max} values of 114 and 117°, respectively. The FWHM values are 18 and 15°, whereas for ClayFF-orig the ∠AlOH^{max} is 135° and the FWHM is 34° (Figure 4c). Understandably, the Al−O−H angle distribution is not significantly affected by the $\theta_{0,SiOH}$ value.

Al−OH and Al−OH_2 Coordination on the AC_2 Surface. No migration of OH groups was observed during the DFT-MD or CMD simulations from any kaolinite edge surface. Similarly, on the AC_1 surface, no H_2O desorption was observed with either DFT-MD or CMD set of simulations. DFT-MD does not predict any H_2O or OH desorption with a total Al−$O_{surface}$ coordination number equal to 2.00 (i.e., a total Al−O coordination of 6.00). Proton transfer events observed during DFT-MD simulations result in an Al−OH_2 coordination number of 1.41 compared to 1.00 in the pre-equilibrated structure (Figure 6).

Some of the initially adsorbed H_2O molecules were later desorbed during the CMD simulations, as illustrated by the Al−O_{H_2O} coordination numbers of 0.00, 0.37, and 0.41 obtained, respectively, by ClayFF-orig, ClayFF-MOH with $\theta_{0,SiOH}$ = 100°, and ClayFF-MOH with $\theta_{0,SiOH}$ = 110° (Figure 6). Contrary to the ClayFF-orig results, the ClayFF-MOH results are in agreement with previous DFT calculations predicting that 5- and 6-coordinated Al atoms should be present on the surface.[44] These results indicate the insufficient time scale of the unconstrained DFT-MD simulations to correctly model this process: during equilibration, several hundred ps were necessary to reach a stable configuration in the repartitioning of adsorbed and desorbed H_2O molecules.

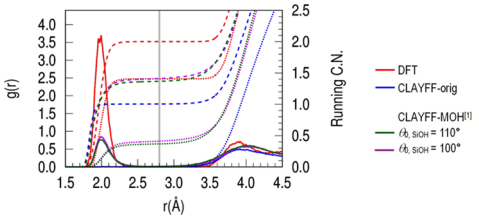

Figure 6. Radial distribution functions (solid lines) and running coordination numbers for Al−O_{H_2O} (dotted lines) and Al−$O_{(H_2O+OH)}$ (dashed lines) at the kaolinite edge surfaces. The vertical gray line indicates the cutoff distance used to determine the first neighbor coordination numbers mentioned in the text.[1] $\theta_{0,AlOH}$ = 110° and k_{SiOH} = k_{AlOH} = 15 kcal mol^{-1} rad^{-2}.

Additionally, if the angle bending term is turned off for bulk Al−OH groups but preserved for surface groups, then all H_2O molecules are desorbed. Therefore, the interaction between kaolinite basal layers, affected by the angle bending term when it is applied to bulk Al−OH groups, influences surface properties. One can assume that strengthening the layer-to-layer H-bonding due to the M−O−H term also facilitates strengthening of the hydrogen bonding network on the edge surface.

Hydrogen Bonding at the Hydrated Kaolinite Edge Surfaces. One of the geometric criteria used to assess if two species are hydrogen bonded is the $H_{donor}\cdots O_{acceptor}$ distance, whose cutoff can be obtained from the position of the first minimum of the corresponding donor−acceptor radial distribution functions. In the current work, depending on the hydrogen bond (HB) donor−acceptor pair and the modeling method, this minimum—usually clearly visible—varies between 2.3 and 2.6 Å (see Figure S1 of the Supporting Information). Therefore, for all HB pairs, we consider a uniform $H\cdots O_{acceptor}$ cutoff distance of R_{HB} = 2.45 Å, which is also the generally accepted value for water−water H-bonds.[61] Additionally, for all the reported HBs, the average O_{donor}−H$\cdots O_{acceptor}$ angle was greater than 130°, which is also consistent with the angular range of HBs in bulk liquid water (see, e.g., ref 62).

Hydrogen bonding at the edge surfaces of kaolinite has previously been studied by means of DFT-MD simulations.[44] Here, HBs significantly affected by the M−O−H term are those involving Al−OH and Si−OH groups; therefore, H-bonding between H_2O molecules and Al−OH_2 groups on both edge surfaces or apical O (Al−O−Si) on the AC_1 surface will not be discussed.

The new angle bending parameterization does not significantly affect the H-bond lengths, which are already satisfactorily close to the DFT results with the ClayFF-orig model (i.e., within 0.10 Å for most HBs). The difference between DFT and ClayFF-orig results in terms of H-bonding essentially lies in the number of H-bonds formed (NHB), which is calculated here as the running coordination number of the donor−acceptor pairs from the corresponding radial distribution functions and using the R_{HB} cutoff distance. The NHB values are reported in Table 3.

DOI: 10.1021/acs.jpcc.9b00514
J. Phys. Chem. C 2019, 123, 11628−11638

Table 3. Average Number of HBs (NHB) for Different Donor−Acceptor HB Pairs at the Kaolinite AC_1 and AC_2 Edge Surfaces

donor	acceptor	DFT[a] current work	DFT[b]	ClayFF-orig	ClayFF-MOH[c]	ClayFF-MOH[d]
			Bulk			
$_{Al_2}$OH	$_{Si}$O$_{Si}$					
			AC_1			
$_{Al}$OH$_2$	$_{Si}$OH	0.12		0.07[e]	0.70	0.67
water	$_{Si}$OH	1.05	∼1.0	0.65	0.81	0.69
$_{Si}$OH	water	0.99	∼1.0	0.86	0.97	0.93
all	$_{Si}$OH	1.17		0.72	1.52	1.36
			AC_2			
$_{Al}$OH$_2$	$_{Si}$OH	0.62		0.00	0.19	0.29
water	$_{Si}$OH	0.37		0.19	0.61	0.75
$_{Si}$OH	water	0.33	0.0 (5-c.) 1.0 (6-c.)	0.76	0.56	0.38
$_{Si}$OH	$_{Al}$OH	0.61		0.08	0.27	0.49
water	$_{Al}$OH	1.33	1.0 (6-c.) 1.8 (5-c.)	1.60	1.64	1.42
$_{Al}$OH	water	0.79	1.0 (6-c.) 0.8 (5-c.)	0.79	0.61	0.73
All	$_{Si}$OH	0.99		0.21	1.00	1.10
$_{Si}$OH	All	0.94		0.84	0.83	0.86
All	$_{Al}$OH	1.95		1.67	1.91	1.90
$_{Al}$OH	all	0.79		0.81	0.81	0.79

[a]HB types with NHB < 0.10 by DFT-MD are not shown here. [b]Estimated from the results of Liu et al.;[44] values for both 5-coordinate and 6-coordinate edge Al atoms are shown. [c]$\theta_{0,SiOH}$ = 110°, $\theta_{0,AlOH}$ = 110° and k_{SiOH} = k_{AlOH} = 15 kcal mol^{-1} rad^{-2}. [d]$\theta_{0,SiOH}$ = 100°, $\theta_{0,AlOH}$ = 110° and k_{SiOH} = k_{AlOH} = 15 kcal mol^{-1} rad^{-2}. [e]For ClayFF-MOH results, the NHBs within 0.20 units of the DFT-MD values are underlined.

AC_1 Surface. DFT-MD simulations predict that on the AC_1 surface, Si−OH groups donate and accept 1.0 HB from bulk H_2O molecules, in agreement with the previous DFT-MD study.[44] CMD simulations with the three FF versions underestimate the NHB. ClayFF-MOH with $\theta_{0,SiOH}$ = 110° gives the closest NHB values to the DFT-MD ones: 0.81 and 0.97 for donated and accepted HBs, respectively (Table 3).

The HBs donated by Al−OH_2 groups to Si−OH groups occur between different layers at the kaolinite edge surface; therefore, the NHB depends on the alignment between layers. When the layers are perfectly aligned (e.g., 2-layer model used in DFT calculations, Figure 3a), these HBs are not favored (NHB = 0.12). However, if there is a slight shift between the layers (as it is observed in the CMD simulations for a 4-layer model), and the most probable orientation of Si−O−H groups is shifted slightly downward with the ClayFF-MOH parametrization (Figure 5a), then Al−OH_2 groups can donate HBs to Si−OH (Table 3, NHB = 0.67−0.70). Of course, the real alignment heterogeneity of the kaolinite layers in laboratory samples cannot be correctly captured by a simple 2-layer structural model used for DFT-MD simulations.

AC_2 Surface. The H-bonding topologies of the AC_2 surface differ between DFT-MD and CMD in two ways: (i) H_2O desorption is observed only by CMD and (ii) proton transfer between Al and Si sites is obviously observed only by DFT-MD. HBs will be necessarily affected by the protonation and coordination of the Al sites and difference in topologies, in addition to the differences inherent in the interaction models.

DFT-MD predicts that Si−OH groups donate 0.61 HBs to the neighboring Al−OH groups and 0.33 HBs to surface H_2O molecules. As previously shown by Liu et al.,[44] when the Al sites are 5-coordinated, the distance between Al−OH groups and Si−O−H groups is too large for the two groups to form a stable H-bond. Since with ClayFF-orig the Al sites are all 5-coordinated, Si−OH groups do not donate HBs to Al−OH groups (NHB = 0.08) in favor of water molecules (NHB = 0.76). The more realistic AC_2 surfaces obtained from ClayFF-MOH feature both 5- and 6-coordinations, and this results in Si−O−H groups donating 0.27 and 0.49 to Al−OH groups for $\theta_{0,SiOH}$ = 110 and 100° parametrizations, respectively.

According to DFT-MD, water molecules interact with the AC_2 surface by H-bonding primarily with Al−OH groups rather than Si−OH groups, and this is particularly true for the H-bonds accepted by M−OH groups: 1.33 HBs are accepted by Al−OH groups from water molecules compared with 0.37 HBs accepted by Si−OH groups. The latter NHB is not well reproduced by ClayFF-MOH (0.61−0.75), but here the classical force field model is not necessarily less realistic than the DFT result since this higher value is correlated with the situation where one of the HBs accepted by the Si−OH group is donated by an Al−OH_2 group from the neighboring layer. Indeed, similar to the AC_1 surface, H-bonding from Al−OH_2 groups to Si−OH groups depends on the registry shift of the kaolinite layers with respect to each other, which is probably incorrectly captured using a relatively small DFT model.

Overall, in terms of hydrogen bonding, $\theta_{0,SiOH}$ = 100° performs better than $\theta_{0,SiOH}$ = 110° on the AC_2 surface, in agreement with the better performance in terms of angle distributions (Figure 4b). The two parameterizations give very similar results for the AC_1 surface.

Regarding H-bonds accepted by Al−OH groups from water molecules, ClayFF-MOH with $\theta_{0,AlOH}$ = 110° clearly improves on ClayFF-orig, with NHB = 1.42.

Effect of the M−O−H Bending Term on the Bulk Crystal Lattice Parameters. Bulk crystal properties are particularly important not only by themselves, but also when they are correlated with surface properties in the context of simulating realistic mineral platelets and specifically non-swelling mineral particles. Obtaining M−O−H bending parameters that result in accurate bulk properties, for example, crystal lattice parameters, is important even if less central than surface properties in the present context. An illustration of the influence of the θ_0 parameter on the lattice parameters of four representative AlOH-containing layered minerals is given in

DOI: 10.1021/acs.jpcc.9b00514
J. Phys. Chem. C 2019, 123, 11628−11638

Table 4. Errors (%, eq 3) of Bulk Crystal Lattice Parameters Calculated by CMD for Four AlOH-Containing Minerals as a Function of the $\theta_{0,AlOH}$ Value with a Constant k_{AlOH} = 15 kcal mol^{-1} rad^{-2}

	θ_0	gibbsite, $Al(OH)_3$[aR]	boehmite, $AlO(OH)$[b]	kaolinite, $Al_2Si_2O_5(OH)_4$[c]	pyrophyllite, $Al_2Si_4O_{10}(OH)_2$[d]
ClayFF-orig		6.97	2.64	0.91	7.59
ClayFF-MOH[e]	100	6.04	2.01[e]	6.44	2.06
	105	4.70	2.01	6.15	1.94
	110	3.29	2.11	5.27	1.87
	115	1.94	2.33	6.51	1.71
	116[f]	1.73	2.33	3.63	1.69
	120	2.12	2.48	1.46	11.19
	125	3.67	2.75	1.21	20.90
	130	5.47	3.12	1.16	10.90

[aR]ef 64. [b]Ref 65. [c]Ref 46. [d]Ref 66. [e]Errors inferior to 2.5% are underlined. [f]This particular $\theta_{0,AlOH}$ value is included because it was mentioned in our previous work.[39]

Table 4. The difference in lattice parameters derived from CMD values with respect to experimental data is based on the lattice vectors ($\mathbf{u}_1$, $\mathbf{u}_2$, $\mathbf{u}_3$)

$$\frac{\sum_{i=1}^{3} \|\mathbf{u}_i - \mathbf{u}_{i\,\mathrm{ref.}}\|}{\sum_{i=1}^{3} \|\mathbf{u}_{i\,\mathrm{ref.}}\|}, \text{ rewith } \|\mathbf{u}_1\| = a,\ \|\mathbf{u}_2\| = b,\ \|\mathbf{u}_3\| = c \tag{3}$$

The data in Table 4 indicate that the bulk lattice parameters show an exceptional dependence on $\theta_{0,AlOH}$. Assuming, quite arbitrarily, that an error of 2.5% or less is acceptable, Table 4 shows that a single $\theta_{0,AlOH}$ value that satisfies this condition for all four minerals cannot be found. However, it is satisfied with $\theta_{0,AlOH}$ = 115−116° for gibbsite, boehmite, and pyrophyllite and with $\theta_{0,AlOH}$ = 120° for gibbsite, boehmite, and kaolinite. Since $\theta_{0,AlOH}$ = 110° is the most appropriate value for surface properties, selecting the same value for the bulk AlOH groups leads to a reduced error with respect to the lattice parameters obtained from ClayFF-orig for gibbsite, boehmite, and pyrophyllite; thus, depending on the desired accuracy, it may be unnecessary to differentiate bulk and surface Al−OH groups in terms of the FF parameters. However, $\theta_{0,AlOH}$ = 116° is the most optimal value for bulk properties, and we recommend this value when separate $\theta_{0,AlOH}$ parameters are desired for bulk and surface Al−OH groups. Further improvement in the accuracy of the FF could involve distinct parameters for bulk and surface, as it was shown for the point charges (e.g., refs 37 and 63).

We note that a more complete study should involve a smaller sampling mesh and include the dependence of the lattice parameters on the force constant k_{AlOH}. However, we can see from Table 4 that, with the exception of kaolinite, at k_{AlOH} = 15 kcal mol^{-1} rad^{-2}, a θ_0 value can always be found that improves the bulk crystal lattice parameters relative to ClayFF-orig. Even for pyrophyllite, where hydrogen bonding is not involved in keeping the layers together, the M−O−H angle bending term affects lattice parameters. In this case, the change in orientation of the intralayer hydroxyl groups is sufficient to slightly distort the siloxane network and, indirectly, cause a modification of the layer-to-layer interaction.

Vibrational Spectra. It is known that the Si−O−H bending vibrations are sensitive to differences of structure and composition of surface hydroxyl groups in materials like silica or zeolites and can be used for quantitative characterization of their surface properties (see, e.g., ref 67). We have calculated the vibrational density of states for the Si−OH groups at the kaolinite edge surfaces from the velocity autocorrelation function $f(t)$ of the corresponding hydrogen atoms. The function $f'(t)$ is further obtained by windowing $f(t)$, with the upper bound set to t_{win} = 1 ps

$$f'(t) = f(t)\sqrt{1 - \frac{t}{t_{win}}} \tag{4}$$

The vibrational density of states $P(\nu)$ is then calculated as

$$P(\nu) = \int [(f'(t)\cos(\omega t))^2 + (f'(t)\sin(\omega t))^2]\mathrm{d}t \tag{5}$$

The vibrational power spectra were derived for H atoms of Si−O−H and Al−O−H edge surface groups from MD trajectories. The most informative range of librational (bending) frequencies is shown in Figure 7 for the (010) kaolinite

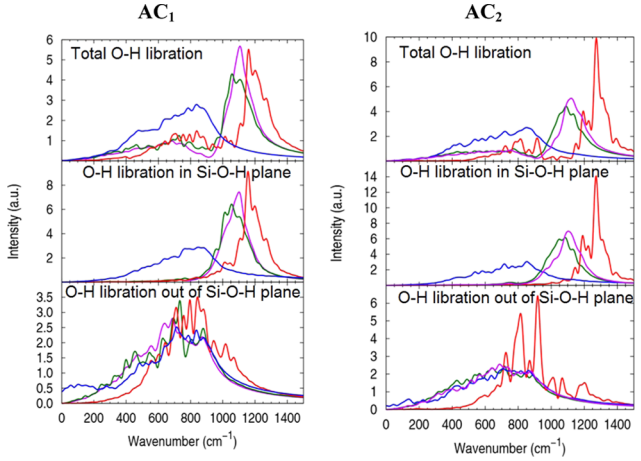

Figure 7. Hydrogen power spectra of the OH groups of the kaolinite AC_1 and AC_2 edge surfaces in the O−H libration region. Color coding of the curves is the same as in Figures 4 and 6.

edges, comparing the performance of the two versions of ClayFF-MOH, ClayFF-orig, with the results of DFT-MD. As seen in the top panel, ClayFF-MOH predicts slightly lower frequencies than DFT-MD for the librational modes of Si−O−H and Al−O−H at higher wavenumbers, whereas these modes are completely missing with ClayFF-orig. After resolving the spectra into in-plane and out-of-plane motion with respect to the equilibrium Si−O−H plane (middle and lower panels, respectively), these higher frequency modes are clearly due to the in-plane Si−O−H bending. At the same time, the librational modes at lower frequency are due to the out-of-plane Si−O−H vibrations and are accurately predicted by

DOI: 10.1021/acs.jpcc.9b00514
J. Phys. Chem. C 2019, 123, 11628−11638

ClayFF with or without the M−O−H angle bending terms. These modes are generally controlled by H-bonding with neighboring surface O−H groups or water molecules.

A detailed analysis of the vibrational behavior of the edge surface hydroxyl groups of kaolinite, including a comparison with available experimental vibrational spectra, is beyond the scope of the current work and will be discussed elsewhere. However, the CMD results presented in Figure 7 based on the comparison with DFT-MD calculations clearly demonstrate a great improvement brought by the addition of the Si−O−H and Al−O−H bending terms for reproducing the librational spectra of the edge O−H groups.

Selection of the Si−O−H Parameters. The overall better performance of $\{\theta_{0,SiOH} = 100°, k_{SiOH} = 15$ kcal mol^{-1} rad$^{-2}\}$ in terms of structural properties of the kaolinite surfaces makes it a better choice than $\{\theta_{0,SiOH} = 110°, k_{SiOH} = 15$ kcal mol^{-1} rad$^{-2}\}$. One could argue from the maps of the mean structural differences (Figure 2) that a decrease in the $\theta_{0,SiOH}$ value from 110 to 100° should be accompanied by a decrease in the k value from 15 kcal mol^{-1} rad^{-2} to 5−10 kcal mol^{-1} rad^{-2}. The pair $\{\theta_{0,SiOH} = 110°, k_{SiOH} = 8$ kcal mol^{-1} rad$^{-2}\}$ was also tested in the simulations, but it only resulted in small structural deviations with respect to $\{\theta_{0,SiOH} = 110°, k_{SiOH} = 15$ kcal mol^{-1} rad$^{-2}\}$, and it worsened the performance in terms of vibrational spectra, shifting the spectra toward lower wavenumbers, as should be expected.

CONCLUSIONS

Combined with the Al−O−H and Mg−O−H angle bending terms from our previous works,[38,39] the present results for the angle bending terms of tetrahedral Si−O−H groups at aluminosilicate edges have been collected in the new ClayFF-MOH parametrization (Table 5). This new functionality enables the simulation of a wide variety of edge−fluid interfaces while maintaining the same degree of lattice flexibility inherent in ClayFF. Additional adjustments may be required for other octahedral or tetrahedral ions such Fe, Al, etc. or for deprotonated sites (AlO^- or SiO^-), but such effort will require spectroscopic results for guidance.

Table 5. Metal−O−H Angle Bending Term Parameters of the Modified ClayFF-MOH Force Field

angle	k (kcal mol^{-1} rad^{-2})	θ_0 (deg)
ao-oh-ho, bulk	15	116
ao-oh-ho, surface	15	110
mg-oh-ho, bulk	6	120
mg-oh-ho, surface	6	110
st-oh-ho	15	100

Table 5 also includes slight adjustments in the octahedral M−O−H equilibrium angle for distinguishing the bulk or surface hydroxyl groups. Additional fine-tuning of angle bending parameters may also be needed to better describe vibrational properties for specific interfaces and may be needed for accurate modeling of local structures at edges or at other silicate surfaces. But for large-scale simulations of clay edges at fluid interfaces, subtle adjustment of M−O−H angle bending parameters will likely have little effect on interfacial properties (e.g., adsorption, diffusion) at longer time and larger length scales. In those cases, the angle bending terms in ClayFF-MOH serve to tether the hydroxyl groups to the edge surfaces, thereby preventing dissociation of these groups, which is beyond the practical scope of a nonreactive force field like ClayFF. Likewise, simulations involving confined shear should be possible with ClayFF-MOH under mild conditions (i.e., elastic regime).

Note that recent kaolinite edge simulations[10] have already demonstrated that inclusion of Si−O−H angle bending parameters, even when unoptimized by comparison with DFT results, allows edge surfaces to be simulated efficiently. The optimized ClayFF-MOH (Table 5) should now be suitable for modeling hydroxylated edge or basal surfaces of clays, related layered minerals, and other aluminosilicate phases. Our goal in developing ClayFF-compatible M−O−H angle bending terms is to faithfully reproduce the structural properties of edge hydroxyl groups in a wide range of interfacial environments. ClayFF can then be used to simulate structural and dynamic properties at edge surfaces as it has been used to simulate basal surfaces since the publication of the original ClayFF parameters in 2004.[29] Spectroscopic determinations of the librational dynamics of M−O−H groups in kaolinite and other clay phases can help evaluate the accuracy of both DFT and new ClayFF parameters, especially in the discrimination of bulk and surface occurrences.

ASSOCIATED CONTENT

Supporting Information

The Supporting Information is available free of charge on the ACS Publications website at DOI: 10.1021/acs.jpcc.9b00514.

Graphs of radial distribution functions (solid lines) and corresponding running coordination numbers (dotted lines) for some donor−acceptor pairs forming H-bonds involving kaolinite hydroxyl groups at the AC_1 and AC_2 edge surface (PDF)

AUTHOR INFORMATION

Corresponding Authors

*E-mail: jagreat@sandia.gov (J.A.G.).
*E-mail: kalinich@subatech.in2p3.fr (A.G.K.).

ORCID

Maxime Pouvreau: 0000-0002-9015-5086
Jeffery A. Greathouse: 0000-0002-4247-3362
Randall T. Cygan: 0000-0003-1262-6177
Andrey G. Kalinichev: 0000-0003-0743-4242

Notes

The authors declare no competing financial interest.

ACKNOWLEDGMENTS

This work was supported by the industrial chair "Storage and Disposal of Radioactive Waste" at the Institut Mines-Télécom Atlantique, funded by ANDRA, Orano, and EDF (A.G.K. and M.P.), and by the U.S. Department of Energy, Office of Science, Office of Basic Energy Sciences, Chemical Sciences, Geosciences, and Biosciences Division (J.A.G. and R.T.C.). A.G.K. also acknowledges the financial support of the European Union's Horizon 2020 research and innovation program under grant agreements Nos 640979 and 764810. Generous allocations of supercomputing resources at the CCIPL, GENCI, and TGCC supercomputing facilities (projects x2014096921, x2015096921, t2016096921, and A0020906921) are also most gratefully acknowledged. Sandia National Laboratories is a multimission laboratory managed and operated by National Technology and Engineering

DOI: 10.1021/acs.jpcc.9b00514
J. Phys. Chem. C 2019, 123, 11628−11638

Solutions of Sandia, LLC., a wholly owned subsidiary of Honeywell International, Inc., for the U.S. Department of Energy's National Nuclear Security Administration under contract DE-NA0003525. The views expressed in this article do not necessarily represent the views of the U.S. Department of Energy or the United States Government.

REFERENCES

(1) Geysermans, P.; Noguera, C. Advances in Atomistic Simulations of Mineral Surfaces. *J. Mater. Chem.* **2009**, *19*, 7807−7821.
(2) Greathouse, J. A.; Johnson, K. L.; Greenwell, H. C. Interaction of Natural Organic Matter with Layered Minerals: Recent Developments in Computational Methods at the Nanoscale. *Minerals* **2014**, *4*, 519−540.
(3) Heinz, H.; Ramezani-Dakhel, H. Simulations of Inorganic-Bioorganic Interfaces to Discover New Materials: Insights, Comparisons to Experiment, Challenges, and Opportunities. *Chem. Soc. Rev.* **2016**, *45*, 412−448.
(4) Kirkpatrick, R. J.; Kalinichev, A. G.; Bowers, G. M.; Yazaydin, A. O.; Krishnan, M.; Saharay, M.; Morrow, C. P. NMR and Computational Molecular Modeling Studies of Mineral Surfaces and Interlayer Galleries: A Review. *Am. Mineral.* **2015**, *100*, 1341−1354.
(5) Martins, M. L.; Gates, W. P.; Michot, L.; Ferrage, E.; Marry, V.; Bordallo, H. N. Neutron Scattering, a Powerful Tool to Study Clay Minerals. *Appl. Clay Sci.* **2014**, *96*, 22−35.
(6) Skipper, N. T.; Lock, P. A.; Titiloye, J. O.; Swenson, J.; Mirza, Z. A.; Howells, W. S.; Fernandez-Alonso, F. The Structure and Dynamics of 2-Dimensional Fluids in Swelling Clays. *Chem. Geol.* **2006**, *230*, 182−196.
(7) Sutton, R.; Sposito, G. Molecular Simulation of Humic Substance-Ca-Montmorillonite Complexes. *Geochim. Cosmochim. Acta* **2006**, *70*, 3566−3581.
(8) Anderson, R. L.; Ratcliffe, I.; Greenwell, H. C.; Williams, P. A.; Cliffe, S.; Coveney, P. V. Clay Swelling - A Challenge in the Oilfield. *Earth-Sci. Rev.* **2010**, *98*, 201−216.
(9) Greathouse, J. A.; Cygan, R. T.; Fredrich, J. T.; Jerauld, G. R. Adsorption of Aqueous Crude Oil Components on the Basal Surfaces of Clay Minerals: Molecular Simulations Including Salinity and Temperature Effects. *J. Phys. Chem. C* **2017**, *121*, 22773−22786.
(10) Zeitler, T. R.; Greathouse, J. A.; Cygan, R. T.; Fredrich, J. T.; Jerauld, G. R. Molecular Dynamics Simulation of Resin Adsorption at Kaolinite Edge Sites: Effect of Surface Deprotonation on Interfacial Structure. *J. Phys. Chem. C* **2017**, *121*, 22787−22796.
(11) Chen, B.; Evans, J. R. G.; Greenwell, H. C.; Boulet, P.; Coveney, P. V.; Bowden, A. A.; Whiting, A. A Critical Appraisal of Polymer-Clay Nanocomposites. *Chem. Soc. Rev.* **2008**, *37*, 568−594.
(12) Cygan, R. T.; Greathouse, J. A.; Heinz, H.; Kalinichev, A. G. Molecular Models and Simulations of Layered Minerals. *J. Mater. Chem.* **2009**, *19*, 2470−2481.
(13) Scocchi, G.; Posocco, P.; Fermeglia, M.; Pricl, S. Polymer-Clay Nanocomposites: A Multiscale Molecular Modeling Approach. *J. Phys. Chem. B* **2007**, *111*, 2143−2151.
(14) Suter, J. L.; Groen, D.; Coveney, P. V. Chemically Specific Multiscale Modeling of Clay-Polymer Nanocomposites Reveals Intercalation Dynamics, Tactoid Self-Assembly and Emergent Materials Properties. *Adv. Mater.* **2015**, *27*, 966−984.
(15) Suter, J. L.; Groen, D.; Coveney, P. V. Mechanism of Exfoliation and Prediction of Materials Properties of Clay-Polymer Nanocomposites from Multiscale Modeling. *Nano Lett.* **2015**, *15*, 8108−8113.
(16) Zeng, Q. H.; Yu, A. B.; Lu, G. Q. Multiscale Modeling and Simulation of Polymer Nanocomposites. *Prog. Polym. Sci.* **2008**, *33*, 191−269.
(17) Aristilde, L.; Marichal, C.; Miehe-Brendle, J.; Lanson, B.; Charlet, L. Interactions of Oxytetracycline with a Smectite Clay: A Spectroscopic Study with Molecular Simulations. *Environ. Sci. Technol.* **2010**, *44*, 7839−7845.
(18) Liu, C.; Li, H.; Johnston, C. T.; Boyd, S. A.; Teppen, B. J. Relating Clay Structural Factors to Dioxin Adsorption by Smectites: Molecular Dynamics Simulations. *Soil Sci. Soc. Am. J.* **2012**, *76*, 110−120.
(19) Okumura, M.; Kerisit, S.; Bourg, I. C.; Lammers, L. N.; Ikeda, T.; Sassi, M.; Rosso, K. M.; Machida, M. Radiocesium Interaction with Clay Minerals: Theory and Simulation Advances Post-Fukushima. *J. Environ. Radioact.* **2018**, *189*, 135−145.
(20) Zhang, C.; Liu, X.; Lu, X.; He, M.; Jan Meijer, E.; Wang, R. Surface Complexation of Heavy Metal Cations on Clay Edges: Insights from First Principles Molecular Dynamics Simulation of Ni(II). *Geochim. Cosmochim. Acta* **2017**, *203*, 54−68.
(21) Psarras, P.; Holmes, R.; Vishal, V.; Wilcox, J. Methane and CO_2 Adsorption Capacities of Kerogen in the Eagle Ford Shale from Molecular Simulation. *Acc. Chem. Res.* **2017**, *50*, 1818−1828.
(22) Rotenberg, B.; Marry, V.; Dufreche, J. F.; Malikova, N.; Giffaut, E.; Turq, P. Modelling Water and Ion Diffusion in Clays: A Multiscale Approach. *C. R. Chim.* **2007**, *10*, 1108−1116.
(23) Ngouana-Wakou, B. F.; Kalinichev, A. G. Structural Arrangements of Isomorphic Substitutions in Smectites: Molecular Simulation of the Swelling Properties, Interlayer Structure, and Dynamics of Hydrated Cs-Montmorillonite Revisited with New Clay Models. *J. Phys. Chem. C* **2014**, *118*, 12758−12773.
(24) Zaunbrecher, L. K.; Cygan, R. T.; Elliott, W. C. Molecular Models of Cesium and Rubidium Adsorption on Weathered Micaceous Minerals. *J. Phys. Chem. A* **2015**, *119*, 5691−5700.
(25) Ma, Z.; Pathegama Gamage, R.; Rathnaweera, T.; Kong, L. Review of Application of Molecular Dynamic Simulations in Geological High-Level Radioactive Waste Disposal. *Appl. Clay Sci.* **2019**, *168*, 436−449.
(26) Arab, M.; Bougeard, D.; Smirnov, K. S. Experimental and Computer Simulation Study of the Vibrational Spectra of Vermiculite. *Phys. Chem. Chem. Phys.* **2002**, *4*, 1957−1963.
(27) Teppen, B. J.; Rasmussen, K. R.; Bertsch, P. M.; Miller, D. M.; Schafer, L. Molecular Dynamics Modeling of Clay Minerals. 1. Gibbsite, Kaolinite, Pyrophillite, and Beidellite. *J. Phys. Chem. B* **1997**, *101*, 1579−1587.
(28) Sainz-Diaz, C. I.; Hernandez-Laguna, A.; Dove, M. T. Modeling of Dioctahedral 2:1 Phyllosilicates by Means of Transferable Empirical Potentials. *Phys. Chem. Miner.* **2001**, *28*, 130−141.
(29) Cygan, R. T.; Liang, J.-J.; Kalinichev, A. G. Molecular Models of Hydroxide, Oxyhydroxide, and Clay Phases and the Development of a General Force Field. *J. Phys. Chem. B* **2004**, *108*, 1255−1266.
(30) Heinz, H.; Lin, T. J.; Mishra, R. K.; Emami, F. S. Thermodynamically Consistent Force Fields for the Assembly of Inorganic, Organic, and Biological Nanostructures: The INTERFACE Force Field. *Langmuir* **2013**, *29*, 1754−1765.
(31) Tesson, S.; Louisfrema, W.; Salanne, M.; Boutin, A.; Ferrage, E.; Rotenberg, B.; Marry, V. Classical Polarizable Force Field To Study Hydrated Charged Clays and Zeolites. *J. Phys. Chem. C* **2018**, *122*, 24690−24704.
(32) Martins, D. M. S.; Molinari, M.; Gonçalves, M. A.; Mirão, J. P.; Parker, S. C. Toward Modeling Clay Mineral Nanoparticles: The Edge Surfaces of Pyrophyllite and Their Interaction with Water. *J. Phys. Chem. C* **2014**, *118*, 27308−27317.
(33) Newton, A. G.; Sposito, G. Molecular Dynamics Simulations of Pyrophyllite Edge Surfaces: Structure, Surface Energies, and Solvent Accessibility. *Clays Clay Miner.* **2015**, *63*, 277−289.
(34) Newton, A. G.; Kwon, K. D.; Cheong, D. K. Edge Structure of Montmorillonite from Atomistic Simulations. *Minerals* **2016**, *6*, 25.
(35) Ho, T. A.; Greathouse, J. A.; Wang, Y.; Criscenti, L. J. Atomistic Structure of Mineral Nano-aggregates from Simulated Compaction and Dewatering. *Sci. Rep.* **2017**, *7*, No. 15286.
(36) Churakov, S. V. Structure and Dynamics of the Water Films Confined between Edges of Pyrophyllite: A First Principle Study. *Geochim. Cosmochim. Acta* **2007**, *71*, 1130−1144.
(37) Lammers, L. N.; Bourg, I. C.; Okumura, M.; Kolluri, K.; Sposito, G.; Machida, M. Molecular Dynamics Simulations of Cesium

DOI: 10.1021/acs.jpcc.9b00514
J. Phys. Chem. C 2019, 123, 11628−11638

Adsorption on Illite Nanoparticles. *J. Colloid Interface Sci.* **2017**, *490*, 608−620.
(38) Zeitler, T. R.; Greathouse, J. A.; Gale, J. D.; Cygan, R. T. Vibrational Analysis of Brucite Surfaces and the Development of an Improved Force Field for Molecular Simulation of Interfaces. *J. Phys. Chem. C* **2014**, *118*, 7946−7953.
(39) Pouvreau, M.; Greathouse, J. A.; Cygan, R. T.; Kalinichev, A. G. Structure of Hydrated Gibbsite and Brucite Edge Surfaces: DFT Results and Further Development of the ClayFF Classical Force Field with Metal−O−H Angle Bending Terms. *J. Phys. Chem. C* **2017**, *121*, 14757−14771.
(40) Cygan, R. T.; Tazaki, K. Interactions of Kaolin Minerals in the Environment. *Elements* **2014**, *10*, 195−200.
(41) Balan, E.; Calas, G.; Bish, D. L. Kaolin-Group Minerals: From Hydrogen-Bonded Layers to Environmental Recorders. *Elements* **2014**, *10*, 183−188.
(42) Brady, P. V.; Cygan, R. T.; Nagy, K. L. Molecular Controls on Kaolinite Surface Charge. *J. Colloid Interface Sci.* **1996**, *183*, 356−364.
(43) Kremleva, A.; Krüger, S.; Rösch, N. Uranyl adsorption at (010) edge surfaces of kaolinite: A density functional study. *Geochim. Cosmochim. Acta* **2011**, *75*, 706−718.
(44) Liu, X. D.; Lu, X. C.; Wang, R. C.; Meijer, E. J.; Zhou, H. Q.; He, H. P. Atomic Scale Structures of Interfaces between Kaolinite Edges and Water. *Geochim. Cosmochim. Acta* **2012**, *92*, 233−242.
(45) Liu, X. D.; Lu, X. C.; Sprik, M.; Cheng, J.; Meijer, E. J.; Wang, R. C. Acidity of Edge Surface Sites of Montmorillonite and Kaolinite. *Geochim. Cosmochim. Acta* **2013**, *117*, 180−190.
(46) Neder, R. B.; Burghammer, M.; Grasl, T.; Schulz, H.; Bram, A.; Fiedler, S. Refinement of the Kaolinite Structure from Single-Crystal Synchrotron Data. *Clays Clay Miner.* **1999**, *47*, 487−494.
(47) Bish, D. L. Rietveld refinement of the kaolinite structure at 1.5 K. *Clays Clay Miner.* **1993**, *41*, 738−744.
(48) Kameda, J.; Yamagishi, A.; Kogure, T. Morphological Characteristics of Ordered Kaolinite: Investigation Using Electron Back-Scattered Diffraction. *Am. Mineral.* **2005**, *90*, 1462−1465.
(49) White, G.; Zelazny, L. Analysis and Implications of the Edge Structure of Dioctahedral Phyllosilicates. *Clays Clay Miner.* **1988**, *36*, 141−146.
(50) Grimme, S.; Antony, J.; Ehrlich, S.; Krieg, H. A Consistent and Accurate Ab Initio Parametrization of Density Functional Dispersion Correction (DFT-D) for the 94 Elements H-Pu. *J. Chem. Phys.* **2010**, *132*, No. 154104.
(51) VandeVondele, J.; Krack, M.; Mohamed, F.; Parrinello, M.; Chassaing, T.; Hutter, J. Quickstep: Fast and Accurate Density Functional Calculations Using a Mixed Gaussian and Plane Waves Approach. *Comput. Phys. Commun.* **2005**, *167*, 103−128.
(52) VandeVondele, J.; Hutter, J. Gaussian Basis Sets for Accurate Calculations on Molecular Systems in Gas and Condensed Phases. *J. Chem. Phys.* **2007**, *127*, No. 114105.
(53) Goedecker, S.; Teter, M.; Hutter, J. Separable Dual-Space Gaussian Pseudopotentials. *Phys. Rev. B: Condens. Matter Mater. Phys.* **1996**, *54*, 1703−1710.
(54) Greathouse, J. A.; Durkin, J. S.; Larentzos, J. P.; Cygan, R. T. Implementation of a Morse Potential to Model Hydroxyl Behavior in Phyllosilicates. *J. Chem. Phys.* **2009**, *130*, No. 134713.
(55) Berendsen, H. J. C.; Postma, J. P. M.; van Gunsteren, W. F.; Hermans, J. Interaction Models for Water in Relation to Protein Hydration. In *Intermolecular Forces*; Pullman, B., Ed.; The Jerusalem Symposia on Quantum Chemistry and Biochemistry; Springer: Netherlands, 1981; pp 331−342.
(56) Teleman, O.; Jönsson, B.; Engström, S. A Molecular Dynamics Simulation of a Water Model with Intramolecular Degrees of Freedom. *Mol. Phys.* **1987**, *60*, 193−203.
(57) Gale, J. D.; Rohl, A. L. The General Utility Lattice Program (GULP). *Mol. Simul.* **2003**, *29*, 291−341.
(58) Plimpton, S. Fast Parallel Algorithms for Short-Range Molecular Dynamics. *J. Comput. Phys.* **1995**, *117*, 1−19.
(59) Martyna, G. J.; Klein, M. L.; Tuckerman, M. Nosé−Hoover Chains: The Canonical Ensemble via Continuous Dynamics. *J. Chem. Phys.* **1992**, *97*, 2635−2643.
(60) Parrinello, M.; Rahman, A. Polymorphic Transitions in Single Crystals: A New Molecular Dynamics Method. *J. Appl. Phys.* **1981**, *52*, 7182−7190.
(61) Chowdhuri, S.; Chandra, A. Hydrogen Bonds in Aqueous Electrolyte Solutions: Statistics and Dynamics Based on Both Geometric and Energetic Criteria. *Phys. Rev. E* **2002**, *66*, No. 041203.
(62) Kalinichev, A. G. Universality of Hydrogen Bond Distributions in Liquid and Supercritical Water. *J. Mol. Liquids* **2017**, *241*, 1038−1043.
(63) Yu, K. A.; Schmidt, J. R. Elucidating the Crystal Face- and Hydration-Dependent Catalytic Activity of Hydrotalcites in Biodiesel Production. *J. Phys. Chem. C* **2011**, *115*, 1887−1898.
(64) Saalfeld, H.; Wedde, M. Refinement of Crystal-Structure of Gibbsite, $Al(OH)_3$. *Z. Kristallogr.* **1974**, *139*, 129−135.
(65) Corbató, C. E.; Tettenhorst, R. T.; Christoph, G. G. Structure Refinement of Deuterated Boehmite. *Clays Clay Miner.* **1985**, *33*, 71−75.
(66) Lee, J.; Guggenheim, S. Single-Crystal X-Ray Refinement of Pyrophyllite-1tc. *Am. Miner.* **1981**, *66*, 350−357.
(67) Mix, H.; Sauer, J.; Schroder, K. P.; Merkel, A. Vibrational Properties of Surface Hydroxyls: Nonempirical Model-Calculations Including Anharmonicities. *Collect. Czech. Chem. Commun.* **1988**, *53*, 2191−2202.

DOI: 10.1021/acs.jpcc.9b00514
J. Phys. Chem. C 2019, 123, 11628−11638

Structure of Hydrated Kaolinite Edge Surfaces: DFT Results and Further Development of the ClayFF Classical Force Field with Metal-O-H Angle Bending Terms

Supporting information

Maxime Pouvreau,[†,‡] Jeffery A. Greathouse,[*,§] Randall T. Cygan[§], Andrey G. Kalinichev[*,†]

[†]Laboratoire SUBATECH (UMR 6457 - Institut Mines-Télécom Atlantique, Université de Nantes, CNRS/IN2P3), 44307 Nantes, France

[‡]Department of Chemistry, Washington State University, Pullman, Washington 99164, USA

[§]Geochemistry Department, Sandia National Laboratories, P.O Box 5800, MS 0754, Albuquerque, NM, 87185-0754, USA

[*] Corresponding authors: jagreat@sandia.gov

kalinich@subatech.in2p3.fr

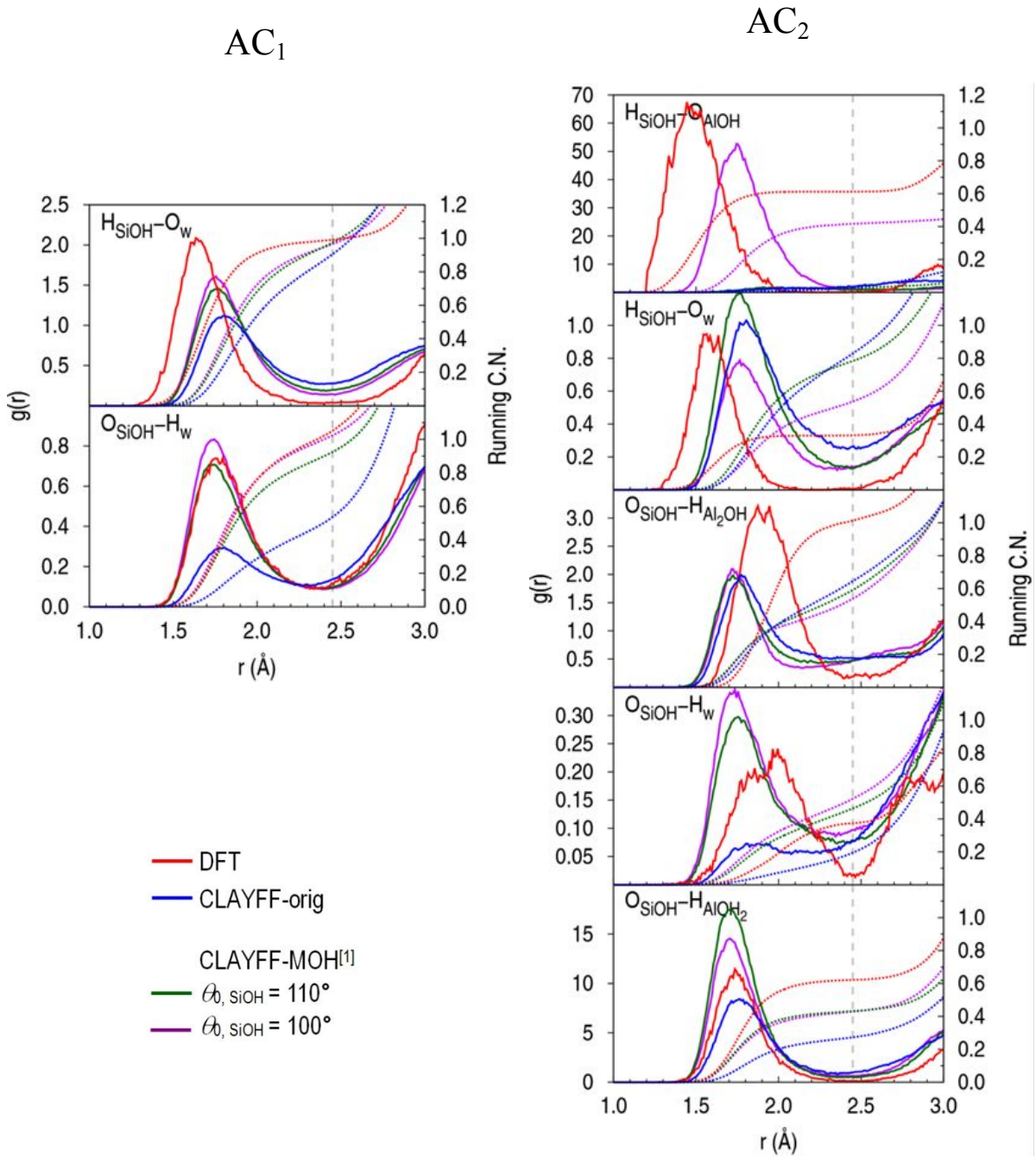

Figure S1. Radial distribution functions (solid lines) and corresponding running coordination numbers (dotted lines) for some donor-acceptor pairs forming H-bonds involving kaolinite hydroxyl groups at the AC_1 and AC_2 edge surfaces. The vertical dashed line shows the distance cutoff R_{HB} = 2.45 Å.

[1] $\theta_{0,\,AlOH}$ = 110° and k_{AlOH} = 15 kcal·mol^{-1}·rad^{-2}.